Electronic Supplementary Material (ESI) for Environmental Science: Advances.


# Visible light-driven degradation of anthracene and naphthalene on robust $Cu^{2+}$-doped ZnO nanoparticles from simulated rainwater: Optimization factors, kinetics, and reusability

Meenu[1], Manviri Rani[1]*, Uma Shanker[2]*

[1]Department of Chemistry
Malaviya National Institute of Technology
Jaipur, Rajasthan, India

[2]Department of Chemistry
Dr. B R Ambedkar National Institute of Technology
Jalandhar, Punjab, India

* Corresponding Author
Dr. Uma Shanker
Office Number-203, New Science Block
Department of Chemistry
Dr. B R Ambedkar National Institute of Technology Jalandhar,
Jalandhar, Punjab, India-144011
Email: shankeru@nitj.ac.in, umaorganic29@gmail.com
Contact number: +91- 7837-588-168 (Mobile)
+91-0181-269-301-2258 (Office)
Fax: +91-0181-269-0932
*Dr. Manviri Rani
Assistant Professor
Department of Chemistry
Malaviya National Institute of Technology
Jaipur, Rajasthan, India-302017
Email: manviri.chy@mnit.ac.in
Contact number: +91-9549650291

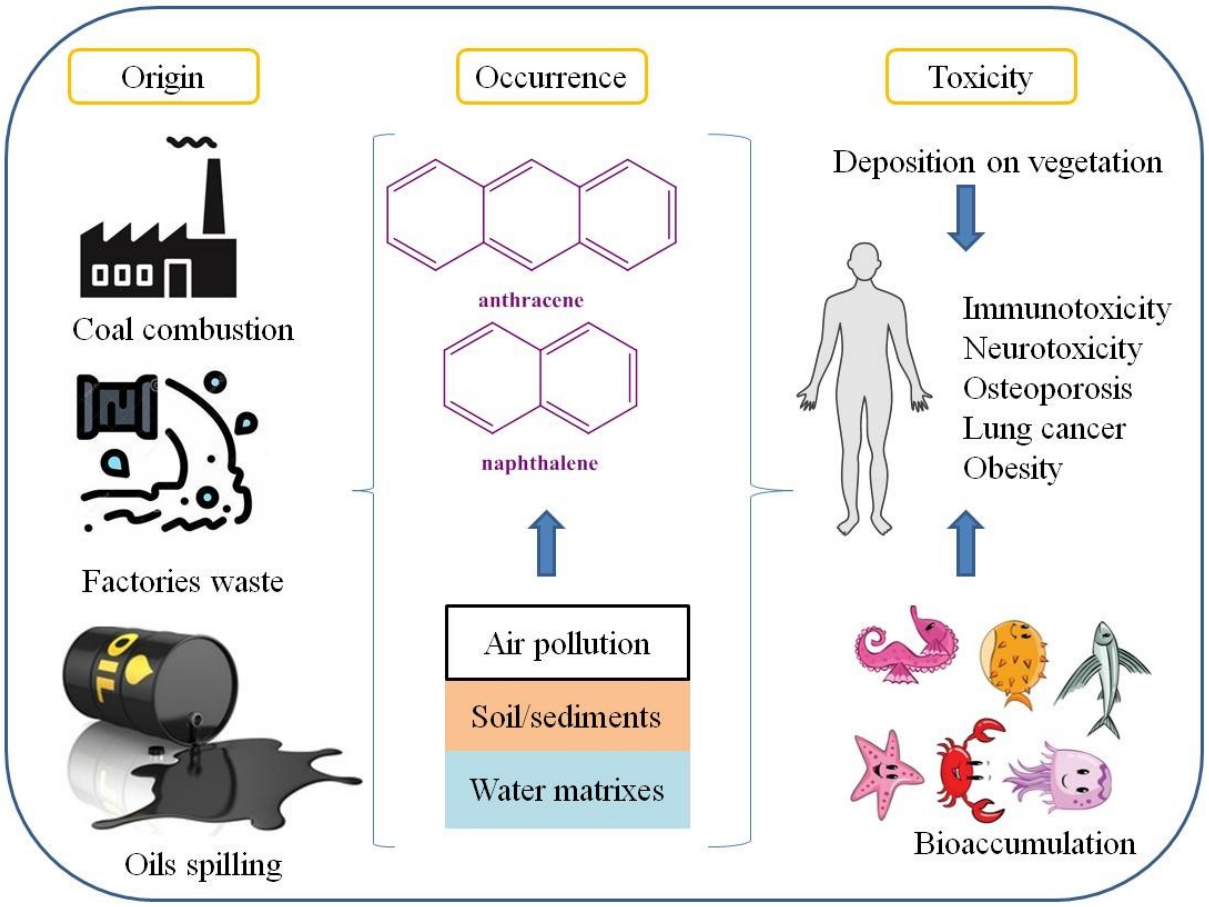


Figure 1S. Risk assessment of anthracene (ANT) and naphthalene (NAP) from production to disposal

**Nanocatalysts Characterization**

Powder X-ray diffraction (PXRD) spectra were obtained using a PAN analytical X-PRT PRO instrument with a CuKα radiation having λ=1.5406 Å. The morphology of the photocatalysts was analyzed by Field-Emission Scanning Electron Microscopy (FE-SEM) using Model JSM6100 (Jeol) with Image Analyser instrument scanning (SEM, Hitachi S4800). Brunauer-Emmett-Teller (BET) specific surface area was obtained by nitrogen adsorption-desorption isotherm analysis using SMART Instruments, SMART SORB 93 model after degassing at 150 °C for 3 hours.

UV–vis absorption spectrophotometer (Shimadzu UV-2401PC) was used to calculate the band gap energy value by converting it into Tauc's plot. Fourier transform infrared spectra (FT-IR) were recorded in the range 400–4000 $cm^{-1}$ (Agilent ATR model) to understand the bonding present in the coordination complex. The stability of the photocatalysts was determined by measuring the zeta potential using Malvern Zetasizer (Zetasizer Ver. 7.11). The absorbance of samples was measured with a UV Spectrophotometer (Agilent Pro).

Table 1S. Shows P-XRD data of Cu@ZnO, and ZnO nanoparticles with their hkl, 2θ (degree), relative intensity [ I %] and d-spacing values, respectively

| **Nanocatalysts** | **hkl** | **d [Å]** | **2θ [°]** | **I [%]** |
|---|---|---|---|---|
| Cu@ZnO | 100 | 2.81112 | 31.807 | 54.6 |
| | 002 | 2.59850 | 34.488 | 39.6 |
| | 101 | 2.47257 | 36.304 | 100.0 |
| | 111 | 2.35681 | 44.184 | 35.5 |
| | 200 | 1.90816 | 47.618 | 21.8 |
| | 102 | 1.89925 | 49.723 | 20.0 |
| | 110 | 1.62300 | 56.668 | 33.1 |
| | 103 | 1.47479 | 62.975 | 30.5 |
| | 112 | 1.40556 | 66.465 | 4.6 |
| | 200 | 1.37655 | 68.054 | 3.6 |
| ZnO | 100 | 2.81112 | 31.807 | 54.6 |
| | 002 | 2.59850 | 34.488 | 39.6 |
| | 101 | 2.47257 | 36.304 | 100.0 |
| | 111 | 1.90816 | 47.618 | 21.8 |
| | 200 | 1.62300 | 56.668 | 33.1 |
| | 103 | 1.47479 | 62.975 | 30.5 |
| | 112 | 1.40556 | 66.465 | 4.6 |

Crystalline size can be calculated using the Scherrer equation i.e.

$$d = \frac{k\lambda}{\beta cos\theta} \text{ ---------- } (Eq1S)$$

where k is constant and its value is 0.9

λ is X-ray wavelength = 1.5 for Cu

β is the FWHM of the peak profile

θ is the diffraction angle of the reflection

The average crystallite size of Cu@ZnO, and ZnO is 25.3 nm, and 23.9nm, respectively.

The broadening and shifting of peaks revealed the crystal lattice refinement along with the strain associated with powder. The strain produced in powdered because of crystal imperfection and distortion was calculated using the formula:

$$\beta_{hkl} = \frac{K\lambda}{D\cos\theta} + 4\epsilon\tan\theta \qquad \text{(Eq2S)}$$

$$\delta = 1/D^2 \qquad \text{(Eq 3S)}$$

Where, $K$ = shape factor (0.9), ε = micro-strain, δ = dislocation density, and λ = wavelength of Cuk radiation (0.154 nm). Plotting between 4 sinθ and $\beta_{hkl}$ cosθ provides crystalline size (intercept) and micro-strain (slope) from eq.2S. The dislocation density for the nanocomposite was calculated by eq. 3S.

Table 2S. Shows the stretching frequency of various functional groups exiting in Cu@ZnO, and ZnO nanoparticles respectively

| **Nanoparticles** | **Functional groups** | **Wave number ($cm^{-1}$)** |
|---|---|---|
| Cu@ZnO | O-H (Stretching) | 3453 |
| | C-H (Stretching) | 2923 |
| | C-H (Deformation) | 2421 |
| | H-O-H (Deformation) | 1641 |
| | C-O (Stretching) | 1510 |

| | | |
|---|---|---|
| | O-H (Deformation) | 1422 |
| | Zn-O-Cu (Stretching) | 1115 |
| | Zn-O (Stretching) | 490 |
| | Cu-O (Stretching) | 435 |
| ZnO | O-H (Stretching) | 3470 |
| | C-H (Stretching) | 2930 |
| | C-O (Stretching) | 1520 |
| | O-H (Deformation) | 1425 |
| | Zn-O-Zn (Stretching) | 1109 |
| | Zn-O (Stretching) | 490 |

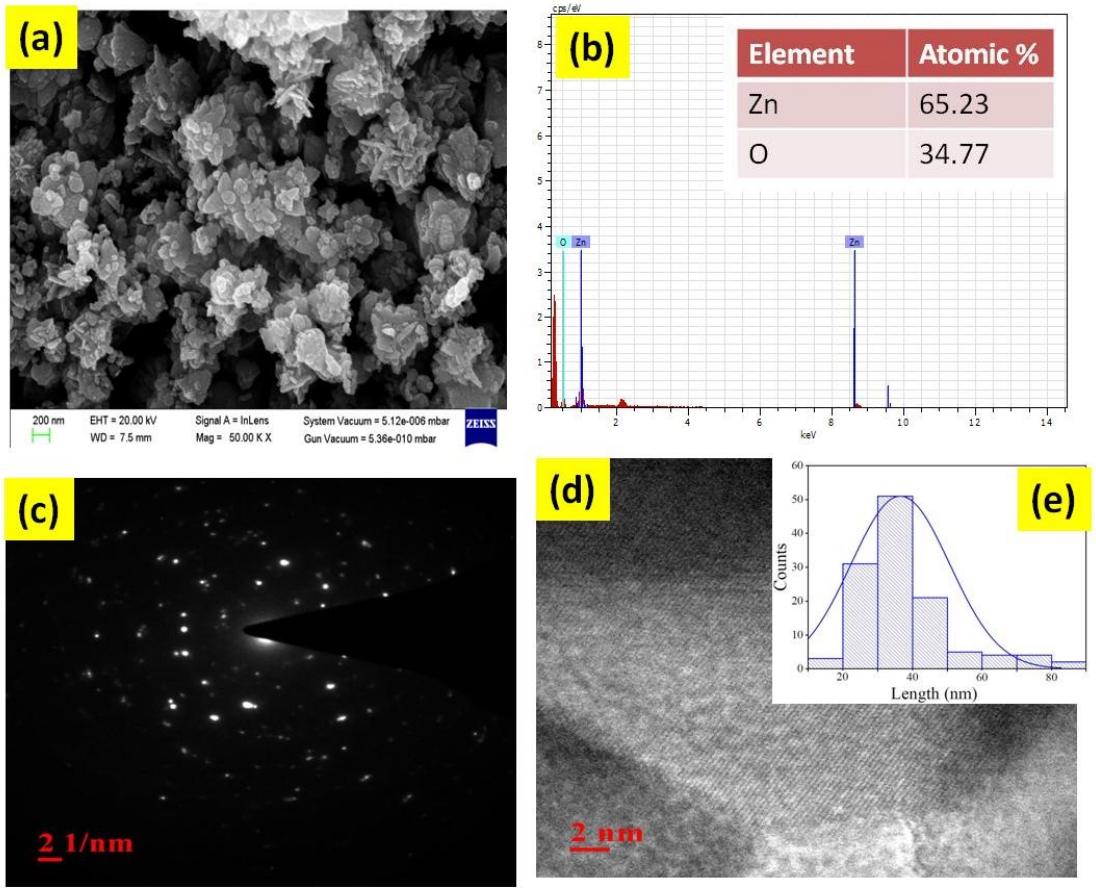


Figure 2S. (a) FE-SEM image (b) EDS spectra with atomic % (c) HR-TEM SEAD pattern, (d) HR-fringes, and (e) size histogram (Inset figure) of ZnO nanoparticles

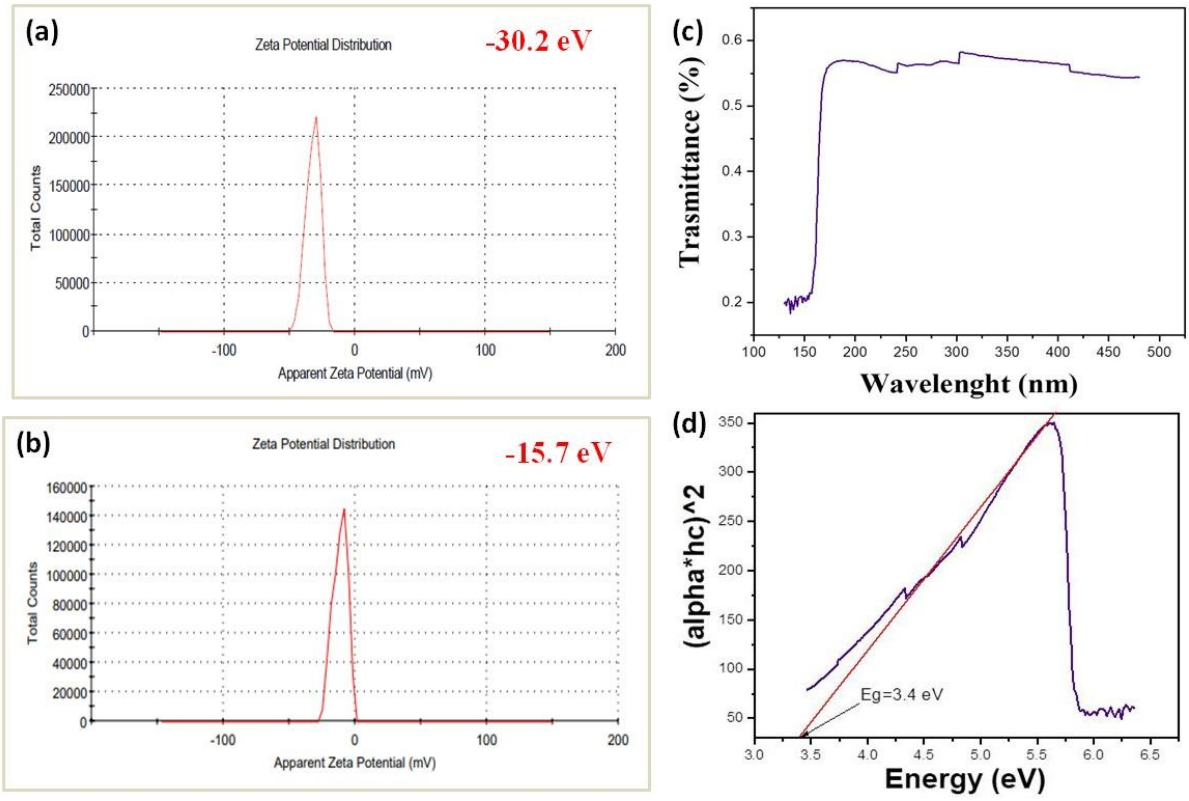


Figure 3S. Zeta potential of (a) Cu@ZnO, (b) ZnO, (c) Uv absorption spectra, and (d) Band gap of ZnO nanoparticles respectively

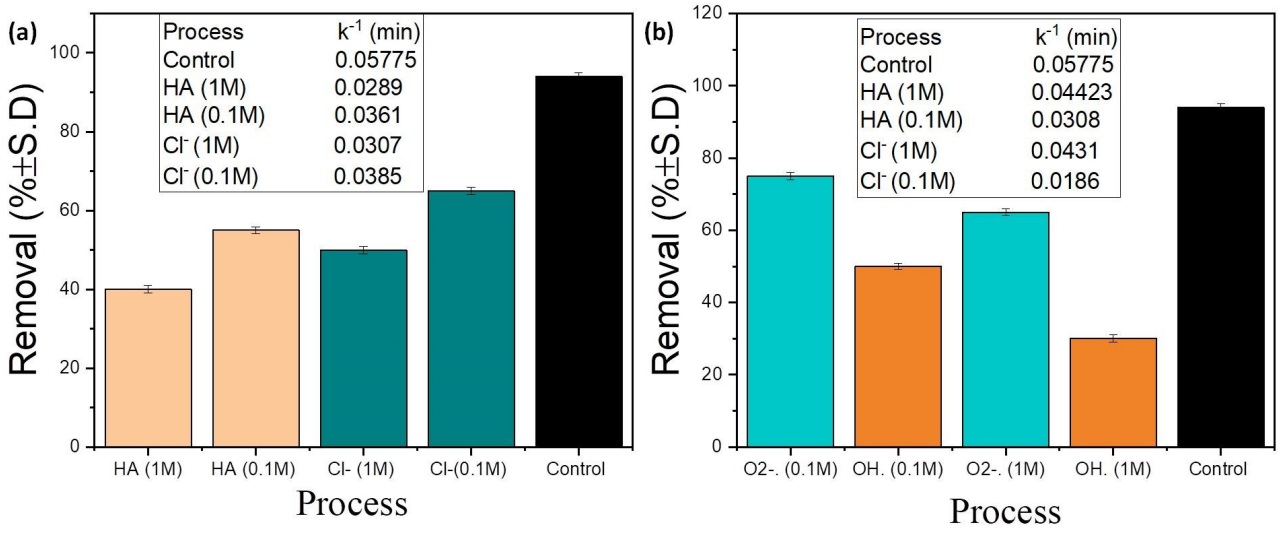

Figure 4S. (a) Humic acid (HA) and Chloride ion ($Cl^-$) (b) Scavenger ion effect on degradation of anthracene by Cu@ZnO nanocomposite (Note: - Triplicate experiments (n=3) were evaluated for estimation of error bar)

**Statistical analysis**

The statistical plots of reaction and kinetics for the degradation of PAHs (ANT&NAP) over the nanocomposites were performed factually from the origin pro 8.5 software. Results stood reproducible for triplicate analysis. The standard deviation of the triplicates was calculated through the Microsoft Excel program. The significance of the results was compared through regression of coefficient ($R^2$) and p-values ($\geq 0.05$). Several adsorptions model data were scrutinized. Linear curves($Y=mX+c$) for adsorption and concentration-dependent study have been obtained while exponential graphs attaining maxima were observed for reduction.

During the kinetic study negative values of time, the removal of the pollutant was achieved by adsorption with a period of 50 min. Therefore, the total removal of PAHs consisted of the contributions from both the adsorption and the photodegradation. The details of the adsorption experiment are given below-

The 10 mg of each adsorbent (Cu@ZnO, and ZnO) was brought into contact with aq. PAHs solution (10 mg $L^{-1}$) and the reaction mixture was agitated at a speed of 400 rpm for 50 min under dark condition. The percentage of PAHs in each of the aliquot samples was determined after 50 min by measuring the difference in absorbance using HPLC (Model: 1260WD). The absorbance ($X_e$) was calculated through the equation (Figure 4S):

$$X_e = \frac{(Ci - Ce) \times Vol\ of\ solution\ (mL) \times Molecular\ weight\ of\ adsorbent}{Amount\ of\ catalyst\ (mg)}$$

Where $C_i$ and $C_e$ are the initial and the equilibrium concentrations of PAHs in mg $L^{-1}$; $X_e$ is the amount of PAHs adsorbed per gm weight of adsorbent (photocatalyst).

Table 3S. Adsorption isotherm (Freundlich, Temkin, Slip, and DRK,) resulted in different $R^2$ and p values of Cu@ZnO, and ZnO

| **Adsorption model** | **Cu@ZnO** | | **ZnO** | |
|---|---|---|---|---|
| | **$R^2$** | **p** | **$R^2$** | **p** |
| **Langmuir** | 0.99 | 0.010 | 0.97 | 0.009 |
| **Freundlich** | 0.93 | 0.0047 | 0.91 | 0.040 |
| **Temkin** | 0.89 | 0.0041 | 0.87 | 0.038 |
| **Slip** | 0.85 | 0.0027 | 0.83 | 0.025 |
| **DR** | 0.80 | 0.0032 | 0.79 | 0.030 |

Adsorption data through Langmuir adsorption isotherms were calculated through the graph of Ce/Xe v/s Ce of the solute. These were calculated by fitting the adsorption data into the equation:

$$\frac{C_e}{X_e} = \frac{1}{k_L X_m} + \frac{C_e}{X_m}$$

or

$$\frac{1}{X_e} = \frac{1}{C_e}\left(\frac{1}{k_L X_m}\right) + \frac{1}{X_m}$$

**Fruendlich Isotherm.**

A typical graph of Xe v/s Ce of the solute was a straight line. $Xe = Kf + Ce1/n$ and the linear form is $\log Xe = \log Kf + \frac{1}{n} logCe$

Where $C_e$ is the equilibrium concentration of the PAHs solution; $X_e$ is the amount of PAHs adsorbed per gram weight of adsorbent; Kf is the Freundlich adsorption constant (mg/g); n is adsorption intensity.

**Temkin Isotherm:**

$$Xe = \frac{RT}{b} \ln A + \frac{RT}{b} \ln Ce$$

Where B=RT/b constant related to the heat of sorption (J/mol) obtained from the Temkin plot (qe VslnCe); A (slope) = Temkin isotherm equilibrium binding constant (L/g); $b$ (intercept) = Temkin isotherm constant; $R$ =universal gas constant (8.314 J·mol−1·K−1) $T$ = Temperature at 298, 308 and 318 K.

As $C_e$ values were very low, the $\ln C_e$ values were coming out to be negative. Therefore, Temkin isotherm ($X_e$ v/s $\ln C_e$) was not plotted for the present study.

**Dubinin-Radushkevich (D-R) isotherm:**

$\ln Xe = \ln Xm$ - $\beta\varepsilon 2$

$$\varepsilon = RT\ ln\left(1 + \frac{1}{Ce}\right)$$

Where $X_m$ is the maximum adsorption capacity (mg/g) obtained from intercept; β ($mol^2/J^2$) is an activity coefficient constant related to sorption energy and obtained from slop;ε is Polanyi potential. D-R was plotted between lnXeVs $\varepsilon^2$

**Sips Isotherm**

It is plotted between 1/Xe $\times 10^{-2}$ (g/mg) and (1/Ce) $\times 10^{-8}$ L/mg; where (1/mg) and (mg/g) are the Sips equilibrium constant and maximum adsorption capacity values obtained from the slope and the intercept of the plot. The Sips isotherm equation is characterized by the dimensionless heterogeneity factor 'n' which can also be employed to describe the system's heterogeneity when is between 0 and 1.

$$\frac{1}{X_e} = \frac{1}{Xm\ Ks}\left(\frac{1}{Ce}\right)1/n + \frac{1}{X_m}$$

Therefore, different adsorption isotherms (Langmuir, Sips, Freundlich, Dubinin-Radushkevich, and Temkin) were investigated (Table 3S and 5S). PAHs eradication was found to be initial adsorption which best fitted the Langmuir adsorption model (Figure 8 a,b). Figure 8c shows the linear fitting of ln(Ct/C0) versus degradation time. The photocatalytic process roughly followed first-order kinetics, which can be expressed as follows: ln(Ct/C0) = kt, where |k| is the apparent rate constant and $C_t$ and $C_0$ are the final and initial concentrations of PAHs, respectively. Both rate constant and rate suggest that PAHs removal was much faster in sunlight than dark i.e.,

photodegradation>>>adsorption. Additionally, nanocomposite shows much more photocatalytic activity compared to individual nanoparticles i.e., Cu@ZnO>ZnO.

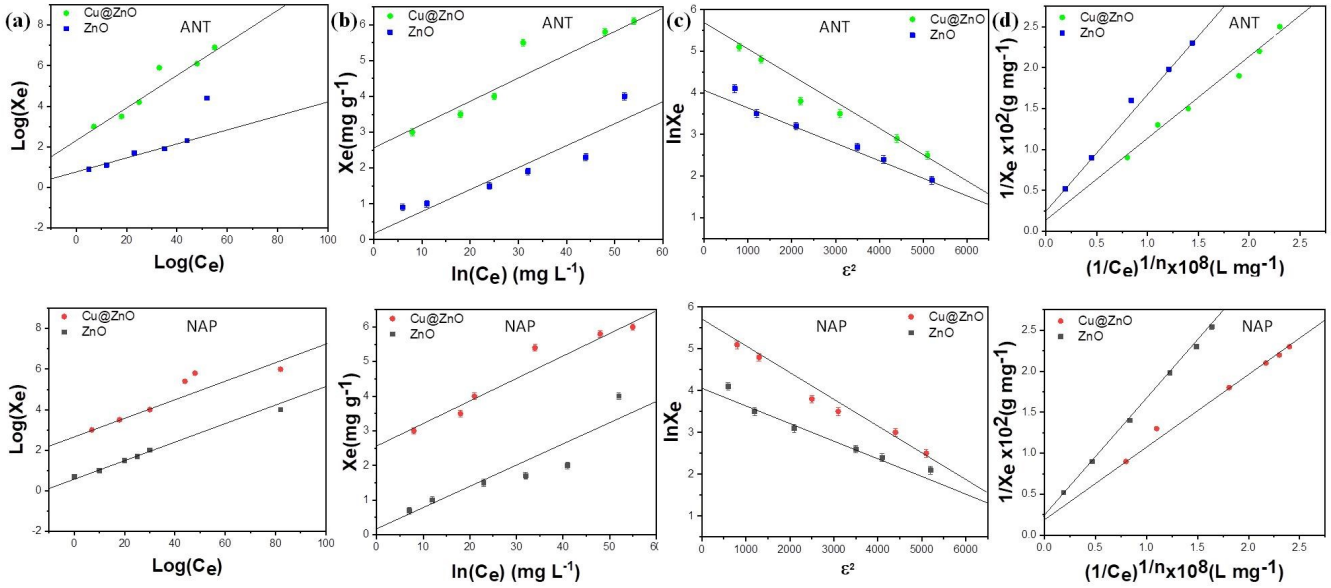


Figure 5S. Adsorption model for PAHs (a) Fruendlich Isotherm, (b) Temkin (c) DRK, (d) Slip, respectively

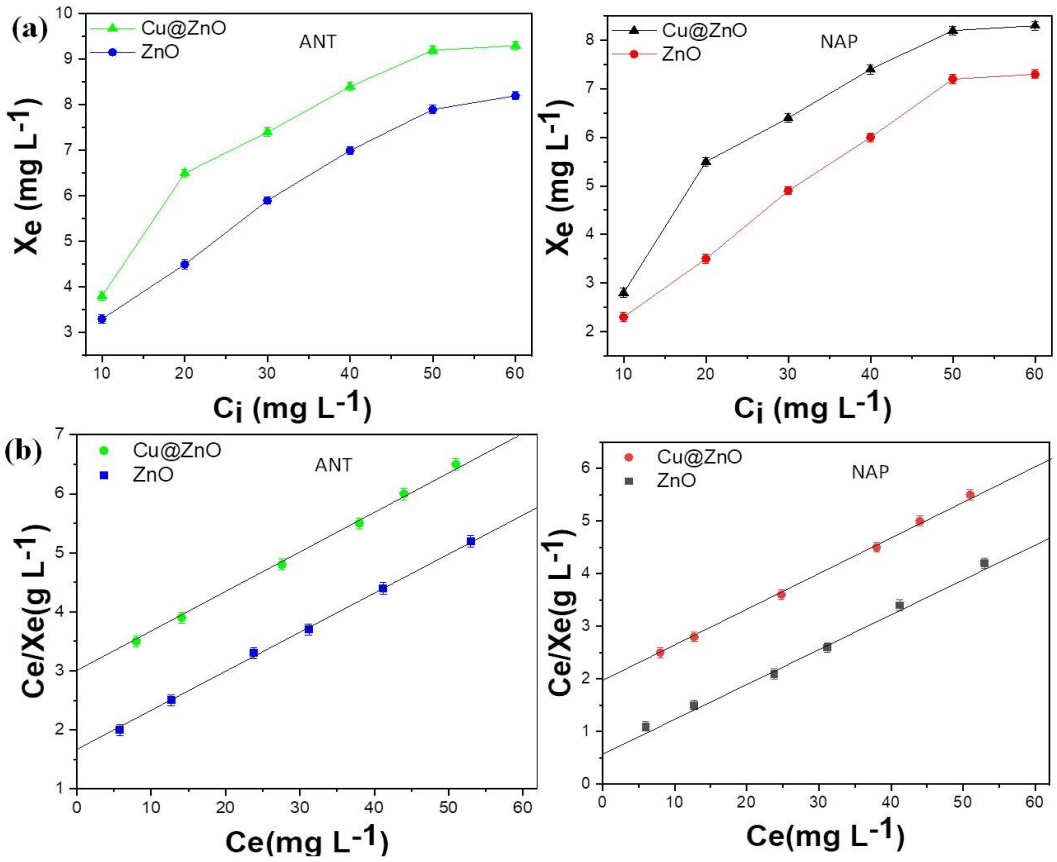


Figure6S. (a) Adsorption isotherm and (b) Langmuir adsorption model for adsorption of PAHs over Cu@ZnO nanocomposite

**Detailed Photo catalytical Degradation Mechanism of ANT and NAP**

The complete removal process is often divided into two steps: initial adsorption of pollutants on nanocatalyst surfaces, and then photocatalytic disintegration by reactive oxygen species generated by the semiconducting characteristics of nanocatalysts. Adsorption occurs in four stages: medium rebellion, particle diffusion, transfers of mass, and bonding to the surface of the photocatalyst. Mass transfer, which was restricted by diffusion resistance, and adsorption on the active sites of the nanocatalysts were used in the removal process.[37] The three stages in photocatalytic degradation that result in active species such as hydroxyl radicals are adsorption, light adsorption, and charge transfer.[27,42] The adsorption capacity of nanoparticles was increased

by Cu doping due to the large surface area, which also allowed for the rapid transfer of ANT and NAP molecules to active sites. The valence (VB) and conduction (CB) band gap energies of photocatalysts are equivalent to or greater than the photons absorbed by the photocatalytic materials. Photon absorption causes charge separation by excitation of electrons from the VB to the CB and the subsequent formation of positive h+ in the VB (Figure 6c). When sunshine was present, a large number of photons were generated and the resulting hybrid connection regulated the electron and hole life dimensions or charge separation in the CB and VB, respectively. In this study, the lifespan of active species carrying charge influenced the photocatalytic breakdown of ANT and NAP. The decreased intensity of the nanocomposite in photoluminescence (PL) spectra avoids charge recombination (Figure 5d). Lower PL emission intensity resulted in better charge carrier separation and quicker transit. The capacity of the Cu@ZnO nanocomposite to recombine electron and hole pairs was lowered due to inadequate intensity monitoring. Copper provides an extra level for the localization of excited or generated electrons from the ZnO CB and increases the life span as well as shifts the adsorption of light toward the visible region can quickly accept electrons, whereas ZnO has a high electron density and can rapidly give electrons. ZnO (n-type) and Cu came into contact, which resulted in an increase in resistivity, a decrease in the number of n-type donor carriers, and a decrease in charge recombination.[3,4] An interfacial electric field formed where Cu and ZnO interacted. Doping ZnO broadens the charged separation range, reducing e-/h+ recombination (Figure 6c). When extremely reactive holes and water combine, a hydroxyl radical is formed, whereas electrons generate $O^{2-\bullet}$ via their interactions with dissolved oxygen.[5] The oxygen molecules and holes can then interact to produce hydro-peroxyl radicals. In addition to HOO radicals, superoxide anion may generate $HO^{\bullet}$ radicals. The following equation describes the general mechanism of active radical production and degradation:

$Cu@ZnO + hv \longrightarrow h^+ + e^-$

$h^+ + ANT/NAP \longrightarrow$ Degraded Products

$h^+ + H_2O \longrightarrow HO^\bullet + H^+$

$OH^\cdot + ANT/NAP \longrightarrow$ Degraded Products

$e^- + O_2 \longrightarrow O^{2-\bullet}$

$O^{2-\bullet} + ANT/NAP \longrightarrow$ Degraded Products

$\cdot O^{2-\bullet} + H_2O \longrightarrow HO^\bullet + OH^- + ½\ O_2$

**PAHS analysis from real field sample**

The rain wastewater sample (RWWS) was collated from two different time intervals from June to July ((RWWS) from the vicinity of Malaviya Nager, Jaipur inlet to the way to the wastewater treatment plant. The 1000 mL of each RWWS was collected in plastic bottles used for distilled water in the laboratory. The ANT and NAT are common components of petroleum and diesel used in automobiles (Saeedi et al., 2012). Hence, due to via use of automobiles in daily life activities for transport, the amount of ANT and NAP was detected in the RWWS. The occurrences of PAHs in RWWS were also detected by other research groups (Guzel et al., 2022; Walaszek et al., 2018). The collected water sample is centrifuged to remove impurities followed by liquid extraction to concentrate the PAHs and analysis by HPLC. The peaks observed in the HPLC spectrum of RWWS at RT 3.5 min and 1.74 nm confirmed the presence of ANT and NAP respectively (Figure 6S). The PAHs were analyzed with HPLC on a 1260WD HPLC system (Agilent 1200 infinity series) with a G1315D 12600 DAD detector with a detection wavelength

of 230 nm. An amethyst C18-P column (5µm, 4.6 155 × 150 mm) was used as a separation column. The HPLC condition for analysis of PAHs in real rainwater sample; Mobile phase: ACN-MEOH (8:2); flow rate: 1.5 mL min; column temperature: 35°C, UV detection (254 nm).

Table 4S. The main characteristics of the real rainwater sample.

| **Parameters** | **Values** |
|---|---|
| pH | 6.31 |
| TOC | 57.77 mg $L^{-1}$ |
| $Cl^-$ | 117 mg $L^{-1}$ |
| HA | 6.95 mmol $L^{-1}$ |
| Color | Slight white grey |
| Odor | musty or earthy odor |

**GC-MS**

Degradation products and metabolites were characterized using a gas chromatograph interfaced with a mass-selective detector (Perkin Elmer-Clarus 500). GC was fitted with an Elite-5 capillary column (Crossbond 5% diphenyl and 95% dimethyl polysiloxane; 30 mL× 0.32 mm i.d.× 0.25 µm film thickness, Perkin Elmer™ instrument, Shelton, CT, USA). Helium was used as both the carrier (1 mL $min^{-1}$) and the make-up gas (40 mL $min^{-1}$). The injector in the splitless mode at 250 $^0$C was used. The transfer line temperature was set at 280 $^0$C and oven temperature was programmed from 60 $^0$C (2 min hold) to 300 $^0$C at the rate of 10 $^0$C $min^{-1}$ (5 min hold). The injected volume and scan time were 2 µL and 0.2 s, respectively. Chromatographic data was acquired by recording the full scan mass spectra in the range m/z 50–500. Mass spectra corresponding to identifying chromatographic peaks were interpreted directly according to the

fragments. Chromatographic data acquisition and processing were carried out with Turbo mass software. The total organic carbon (TOC) of the sample was analyzed with VCSN 5000 analyzer (Shimadzu Japan).

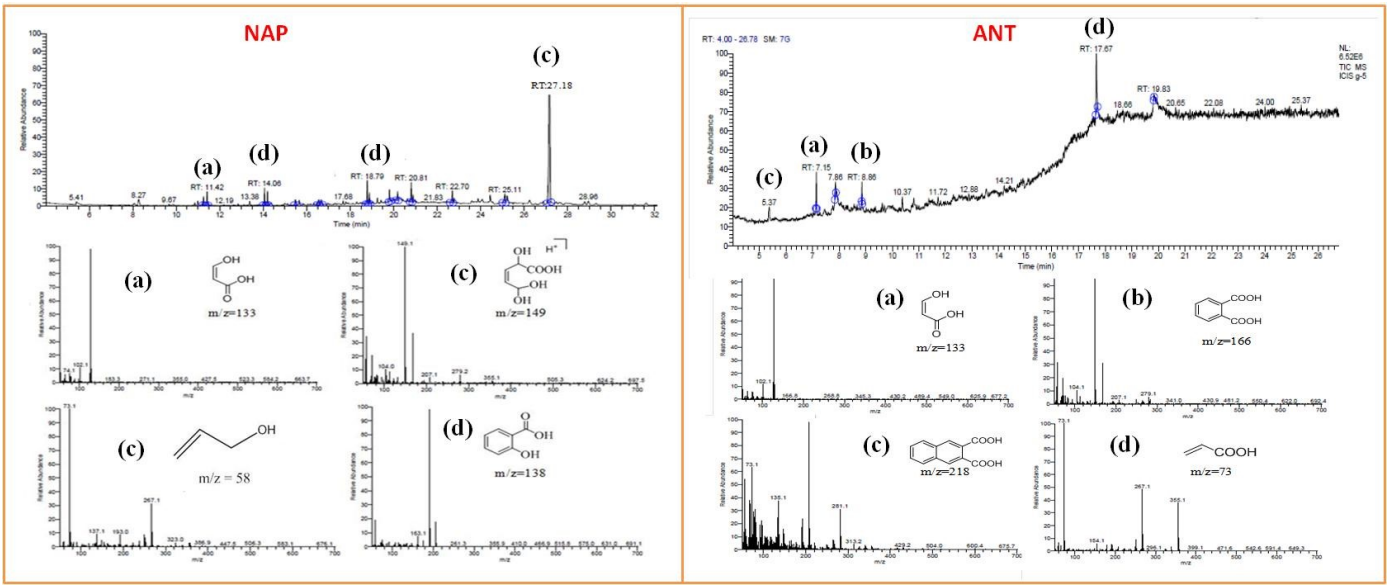


Figure 7S. Representative of Total ion chromatogram (TIC) and mass spectrum of the degraded products formed of naphthalene (NAP) and anthracene (ANT) over Cu@ZnO nanocatalysts (conc; 10mg $L^{-1}$, catalyst dose; 10mg, pH~7, 200min sunlight irridation)